RESEARCH ARTICLE

NANO · MICRO small
www.small-journal.com

Spontaneous-Spin-Polarized 2D π-d Conjugated Frameworks Towards Enhanced Oxygen Evolution Kinetics

Won Seok Lee, Hiroaki Maeda, Yen-Ting Kuo, Koki Muraoka, Naoya Fukui, Kenji Takada, Sono Sasaki, Hiroyasu Masunaga, Akira Nakayama, Hong-Kang Tian, Hiroshi Nishihara,* and Ken Sakaushi**

Alternative strategies to design sustainable-element-based electrocatalysts enhancing oxygen evolution reaction (OER) kinetics are demanded to develop affordable yet high-performance water-electrolyzers for green hydrogen production. Here, it is demonstrated that the spontaneous-spin-polarized 2D π-d conjugated framework comprising abundant elements of nickel and iron with a ratio of Ni:Fe = 1:4 with benzenehexathiol linker (BHT) can improve OER kinetics by its unique electronic property. Among the bimetallic $NiFe_{x:y}$-BHTs with various ratios with Ni:Fe = x:y, the $NiFe_{1:4}$-BHT exhibits the highest OER activity. The $NiFe_{1:4}$-BHT shows a specific current density of 140 A g^{-1} at the overpotential of 350 mV. This performance is one of the best activities among state-of-the-art non-precious OER electrocatalysts and even comparable to that of the platinum-group-metals of RuO_2 and IrO_2. The density functional theory calculations uncover that introducing Ni into the homometallic Fe-BHT (e.g., Ni:Fe = 0:1) can emerge a spontaneous-spin-polarized state. Thus, this material can achieve improved OER kinetics with spin-polarization which previously required external magnetic fields. This work shows that a rational design of 2D π-d conjugated frameworks can be a powerful strategy to synthesize promising electrocatalysts with abundant elements for a wide spectrum of next-generation energy devices.

1. Introduction

Water electrolysis is one of the most promising approaches to producing clean and sustainable hydrogen energy, aiming to achieve carbon neutrality.[1] Water electrolysis accompanies two simultaneous reactions: cathodic hydrogen evolution reaction (HER) and anodic oxygen evolution reaction (OER). OER is a main bottle-neck of water electrolysis as this reaction shows a high overpotential even with the most effective, however, limited-element-based electrocatalysts of iridium or ruthenium.[2] Therefore, a wide spectrum of attempts has been conducted to reduce OER overpotentials by using abundant elements with the hope of paving the way for large-scale green hydrogen production.[3] These OER materials have been designed under the framework of the Sabatier principle.[4] This principle tells us that there is a combination of appropriate adsorption energy on solid surfaces for any reactions, and this adsorption

W. S. Lee, K. Sakaushi
Research Center for Energy and Environmental Materials
National Institute for Materials Science
1-1 Namiki, Tsukuba, Ibaraki 305-0044, Japan
E-mail: sakaushi.ken@nims.go.jp

H. Maeda, N. Fukui, K. Takada, H. Nishihara
Research Institute for Science and Technology
Tokyo University of Science
2641 Yamazaki, Noda, Chiba 278–8510, Japan
E-mail: nisihara@rs.tus.ac.jp

Y.-T. Kuo, H.-K. Tian
Department of Chemical Engineering
National Cheng Kung University
Tainan 70101, Taiwan
E-mail: hktian@gs.ncku.edu.tw

The ORCID identification number(s) for the author(s) of this article can be found under https://doi.org/10.1002/smll.202401987

K. Muraoka, A. Nakayama
Department of Chemical System Engineering
The University of Tokyo
7-3-1 Hongo, Bunkyo-ku, Tokyo 113–8656, Japan

S. Sasaki
Faculty of Fiber Science and Engineering
Kyoto Institute of Technology
Matsugasaki Hashikami-cho 1, Sakyo-ku, Kyoto 606–8585, Japan

S. Sasaki
SPring-8 Center
RIKEN
Kouto 1-1-1, Sayo-cho, Sayo-gun, Hyogo 679–5148, Japan

H. Masunaga
Japan Synchrotron Radiation Research Institute (JASRI)
1-1-1 Kouto, Sayo-cho, Sayo-gun, Hyogo 679–5198, Japan

H.-K. Tian
Hierarchical Green-Energy Materials (Hi-GEM) Research Center
National Cheng Kung University
Tainan 70101, Taiwan

DOI: 10.1002/smll.202401987

energy decides a combination of overpotential and rate-determining steps. Adsorption energy on a solid is essentially decided by a composition of materials: this predicts that if a composition of electrocatalyst is fixed, the fate of a reaction, such as kinetics, selectivity, and overpotential, is decided. As such, aiming to tune the adsorption energies on electrocatalysts, additional external effects, such as light or magnetic field, have been employed in order to develop alternative approaches to material design for enhancing kinetics or selectivity: the former approach is photoelectrochemistry,[5] and latter magnetoelectrochemistry.[6] However, these external energies often require additional extra energy sources or special designs in devices. In consequence, these further efforts often result in additional costs, which is unfavorable to providing green hydrogen at a reasonable price in our society, such as 1 dollar per kilogram.[1b]

Herein we report that a designer material of spontaneous-spin-polarized 2D π-d conjugated framework (2DCF) consisting of abundant elements of iron with benzenehexathiol linker (BHT) is able to improve OER kinetics by its unique electronic property. The density functional theory (DFT) calculations unveiled that a formation of bimetallic 2DCFs by introducing Ni into the Fe-BHT (e.g., Ni:Fe = 0:1) can emerge a spontaneous-spin-polarized state, e.g. a spin-polarization without the addition of external magnetic fields. Thus, these materials can achieve an enhancement OER kinetics as the result of adsorption energy optimization by taking the advantage of the spin-polarization just by the material design, which effect has been believed to be required additional external magnetic field previously. Consequently, the $NiFe_{1:4}$-BHT was found to have the most optimal OER activity, reaching up to 140 A g^{-1} at the overpotential of 350 mV. This performance is one of the best activities among state-of-the-art non-precious OER electrocatalysts and even comparable to that of the platinum-group-metals of RuO_2 and IrO_2.

In this study, we employed the benzenehexathiolato-based 2DCFs as the model material system, which is well-known as the first example of the metallically-conductive coordination framework.[7] As aforementioned, an optimized electronic structure can provide optimal adsorption energies of reaction intermediates, which leads to favorable conditions for the kinetics of electrocatalysis. From this viewpoint, 2DCF is an ideal system as an electronic structure of 2DCF is able to be designed by a wide spectrum of possible combinations in the hybridization of frontier p orbitals of organic linkers with *d* orbitals of transition metal ions.[8] Due to this feature, in addition to high electronic conductivities,[9] 2DCFs have successfully shown various intriguing chemical and physical properties,[10] for instance, rechargeable battery reaction,[11] electrocatalysis,[12] superconductivity,[13] sensing,[14] and thermoelectric materials.[15] We take this advantage of 2DCFs to build up a model electrocatalysis system to study the design strategy on materials with promising OER activity.

2. Results and Discussion

2.1. Building up a Model Electrocatalysis System with 2D π-d Conjugated Framework

Various $NiFe_{x:y}$-BHT samples were synthesized using the interfacial growth method, where a BHT/dichloromethane solution was placed in the bottom of the sample vial, and metal ions in an aqueous solution were added to the upper part (**Figure 1a**).[15] Note that all solutions were degassed with Ar gas, and all processes were conducted in an Ar-filled glove box. Initially, 10 mg of BHT was dissolved in 70 mL of dichloromethane and placed in a 50 mL glass vial (LABCORN). Then, 5 mL of deionized water followed by 5 mL of metal ion-containing aqueous solution (2 x 10^{-3} M) were sequentially added to the BHT/dichloromethane solution. To synthesize various $NiFe_{x:y}$-BHT samples, metal solutions with different Ni (x) to Fe (y) volume ratios (mL:mL) were used: 5:0, 4:1, 3:2, 2:3, 1:4, and 0:5. The samples fabricated using pure Ni or Fe metal aqueous solutions were named Ni-BHT and Fe-BHT, respectively. The samples were allowed to react for 48 h at room temperature to form 2DCF samples in the liquid-liquid interface. As synthesized 2DCF were collected on the glass or silicon substrate for further characterization.

The anodic OER performance of the synthesized 2DCF was first evaluated to screen their potential as an electrocatalyst. Figure S1 (Supporting Information) reveals that the bimetallic $NiFe_{x:y}$-BHTs exhibited more beneficial electrocatalytic properties for OER than the homometallic Ni-BHT and Fe-BHT. Particularly, among the NiFe-BHTs, the $NiFe_{1:4}$-BHT was functionally the most superior. Figure 1b illustrates the potential required to reach 1 mA cm^{-2} of the current density, indicating that the bimetallic $NiFe_{x:y}$-BHTs combinations required a lower potential than homometallic samples, and the $NiFe_{1:4}$-BHT presented the lowest potential. To insightfully understand the unexpected functional benefits of the $NiFe_{1:4}$-BHT, the structure, more detailed electrocatalytic efficiency, and electronic structure based on the DFT were systematically investigated, as shown later.

2.2. Physical Properties of the $NiFe_{x:y}$-BHT

The successful synthesis of 2DCFs was confirmed by the Fourier-transform infrared spectroscopy (FT-IR) and Raman spectroscopy. FT-IR spectrum (Figure S2, Supporting Information) reveals the entire coordination between the S-H groups in the BHT ligands and the metal species. The disappeared signal of the S-H peak in all as-synthesized 2DCF supports this conclusion.[7a] Raman spectra (Figures S3 and S4, Supporting Information) also prove the completed metal-ligand coordination since the vibration peak of the S-H group (≈2500 cm^{-1}) vanished in as-prepared 2DCF samples.[7a] Moreover, the peaks at ≈1120 cm^{-1} and 347/378 cm^{-1} indicate the C—S and S—M bond (Figure S4, Supporting Information), confirming the successful synthesis of 2DCFs.

The information on the structure and orientation of synthesized 2DCFs was characterized by thin-film X-ray diffraction (XRD) techniques and the 2D grazing-incidence wide-angle X-ray scattering (2D GIWAXS) patterns. Thin-film XRD patterns highlight that the Ni-BHT is the most crystalline sample among all the as-synthesized 2DCFs. A pronounced (001) diffraction peak demonstrates a high crystallinity of the Ni-BHT (Figure S5, Supporting Information), consistent with the liquid-liquid interface growth method to produce the vertically stacked 2D planes. Additional characterization by the 2D GIWAXS technique was conducted with the as-synthesized Ni-BHT, Fe-BHT, and $NiFe_{x:y}$-

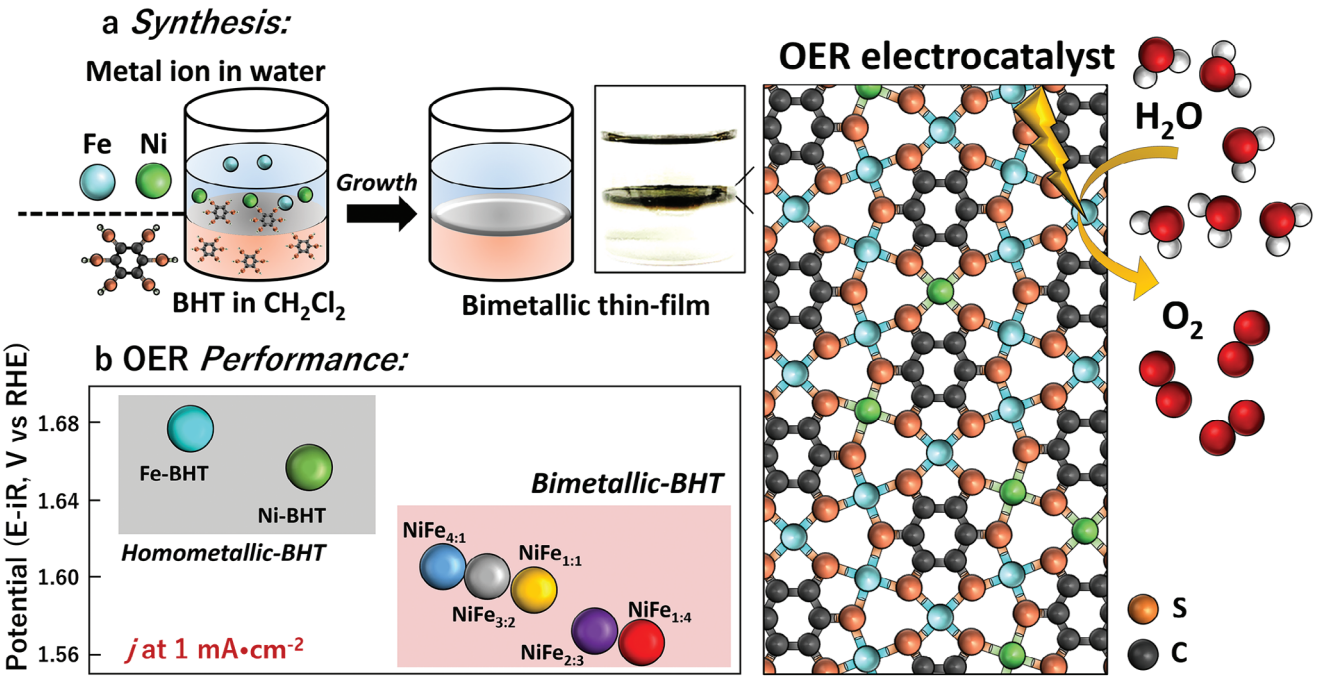

Figure 1. a) Schematic description of the interfacial growth method to produce thin-film 2DCF for OER. b) Electrocatalytic OER performance comparison of as-synthesized thin-film 2DCF electrocatalysts at a current density of 1 mA cm^{-2}, data obtained from LSV curves.

BHT. **Figure** 2a shows an evident (001) diffraction peak in all as-synthesized 2DCFs, showing their layered structure character. The narrowest and sharpest diffraction peak in Ni-BHT further exhibits its high crystallinity. Figure 2b displays a pronounced ring-shaped (001) scattering phenomenon in the 2D GIWAXS pattern of Ni-BHT, relating to the π stacking direction.[15] 2D GIWAXS patterns also clearly reflect that the introduction of Fe species destroyed the growth orientation of the 2DCF, and the crystallinity deteriorated as Fe ratio increased (Figure 2b–h). Particularly, the $NiFe_{1:4}$-BHT exhibited the most inferior crystallinity because of the absence of ring-shaped scattering backgrounds (Figure 2g).

The morphology of as-synthesized 2DCFs was evaluated by using a transmission electron microscope (TEM). The highly crystalline and layered structure of the Ni-BHT is visualized by the TEM images (**Figure** 3a,b). In contrast, a disordered layered structure is displayed in the Fe-BHT (Figure 3c,d) and the $NiFe_{1:4}$-BHT (Figure 3e,f). These results are agreed with the aforementioned diffraction experiments (Figure 2). The energy-dispersive X-ray (EDX) scanning spectra collected from different areas confirmed that Fe is the dominant metal species in $NiFe_{1:4}$-BHT (Figure S6, Supporting Information). In addition, the atomic ratio between Ni and Fe species was confirmed by the inductively coupled plasma mass spectrometry (ICP-MS), and the Ni:Fe atomic ratio of the as-synthesized $NiFe_{1:4}$-BHT was confirmed to be 1.2:4 (Table S1, Supporting Information), which is very close to the theoretical ratio of 1:4.

The chemical bonding environments in the Ni-BHT, the Fe-BHT, the $NiFe_{4:1}$-BHT, and the $NiFe_{1:4}$-BHT were investigated using the X-ray photoelectron spectroscopic (XPS) technique. Figure S7 (Supporting Information) shows the XPS full survey spectra, revealing Ni, Fe, C, and S as the major elements. **Figure** 4a displays the Ni spectra of the Ni species-contained 2DCF (i.e., the Ni-BHT, the $NiFe_{1:4}$-BHT, and the $NiFe_{4:1}$-BHT). The two characteristic peaks ≈871.2 and ≈854.1 eV correspond to the Ni $2p_{1/2}$ and the Ni $2p_{3/2}$, respectively.[15] Similarly, Figure 4b exhibits the Fe spectra of Fe species-contained 2DCF (i.e., the Fe-BHT, the $NiFe_{1:4}$-BHT, and the $NiFe_{4:1}$-BHT). Two peaks at ≈724.9 and 711.3 eV correspond to the signals of the Fe $2p_{1/2}$ and the Fe $2p_{3/2}$, respectively.[16] Furthermore, as shown in Figure 4a,b, the peak position of the bimetallic $NiFe_{xy}$-BHT shifted compared to the parent Ni-BHT and Fe-BHT. In the case of the $NiFe_{4:1}$-BHT, the binding energy of Fe $2p_{3/2}$ peak increased (≈713.0 eV) compared to the Fe-BHT (≈711.1 eV) (Figure 4b), implying that Fe complex tends to donate electrons to the neighboring Ni or S complex (Figure 4d). The binding energy of Ni $2p_{3/2}$ (≈853.9 eV) (Figure 4a) and S 2s (≈227.1 eV) (Figure 4c) did not exhibit considerable peak shifts from those of parent Ni-BHT than the case of Fe $2p_{3/2}$. This result suggests that the charge from Fe was donated to Ni and S complexes. For the $NiFe_{1:4}$-BHT, the binding energy of Fe $2p_{3/2}$ peak (≈711.8 eV) did not show a significant peak shift (Figure 4b). However, the emergence of a wide peak (≈856.0 eV) of Ni $2p_{3/2}$ was observed (Figure 4a), and the binding energy of S 2s (≈227.6 eV) did not shift dramatically compared to that of parent Fe-BHT (Figure 4c). This indicates that Ni could donate charge to Fe and S complexes (Figure 4d). Collectively, the heterometallic 2DCF exhibited an aspect of following the chemical environment of each parent homometallic 2DCF by the charge donation of the metal ion with a small amount. Furthermore, the shifted binding energy of S2s in the $NiFe_{1:4}$-BHT (≈227.6 eV) compared to that of the Ni-BHT (≈227.1 eV) infers that the valence oxidation state of Ni-complex in the $NiFe_{1:4}$-BHT is transitioned,[7a,15] suggesting a highly unsaturated valence oxidation state of the Ni atom in the $NiFe_{1:4}$-BHT.

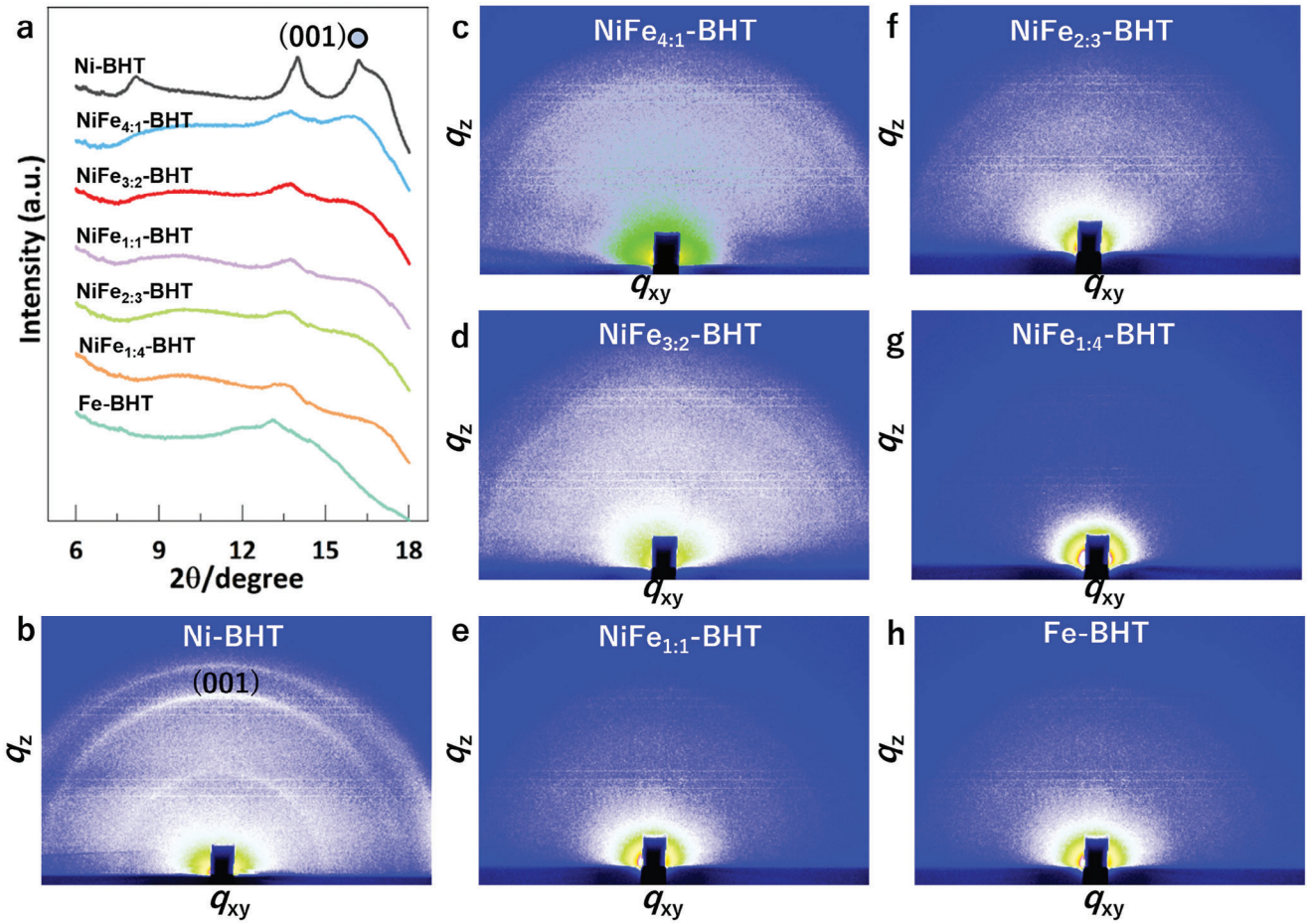

Figure 2. a) XRD patterns of the Ni-BHT, the NiFe-BHT, and the Fe-BHT 2DCF converted from 2D GIWAXS patterns. 2D GIWAXS patterns of b) the Ni-BHT, c) the $NiFe_{4:1}$-BHT, d) the $NiFe_{3:2}$-BHT, e) the $NiFe_{1:1}$-BHT, f) the $NiFe_{2:3}$-BHT, g) the $NiFe_{1:4}$-BHT, and h) the Fe-BHT 2DCF.

2.3. Electrochemical Properties of $NiFe_{x:y}$-BHT

The OER activities of the $NiFe_{x:y}$-BHTs were evaluated in an alkaline electrolyte (0.1 M KOH solution, pH 13). As checked in Figure S1 (Supporting Information), the $NiFe_{1:4}$-BHT exhibited the lowest overpotential to reach the highest OER current density among the $NiFe_{x:y}$-BHTs, also demonstrating the superior electrochemical property compared to the parent homometallic Ni-BHT and Fe-BHT. According to the XPS analysis already shown in Figure 4, $NiFe_{1:4}$-BHT highlighted its potential that the incorporation of Ni species into Fe-BHT can change its electronic properties, in turn leading to significantly improved OER performance. This exceptional performance of the $NiFe_{1:4}$-BHT is clearly illustrated by surpassing that of homometallic Ni-BHT and Fe-BHT 2DCF, and other bimetallic ones (**Figure 5**a,b). The overpotential for reaching OER current density of 10 mA cm^{-2} was 412, 369, and 364 mV for the $NiFe_{3:2}$-BHT, the $NiFe_{1:1}$-BHT, and the $NiFe_{2:3}$-BHT, respectively (Figure 5a). For the bimetallic NiFe-BHT 2DCF, the OER activity depended on the ratio of Fe; however, it did not exhibit a monotonic trend (Figure 5b). Particularly, the heterometallic $NiFe_{1:4}$-BHT 2DCF, containing 76.9% of Fe ratio (Table S1, Supporting Information), demonstrated the most optimized OER activity as an electrocatalyst. In stark comparison, the $NiFe_{4:1}$-BHT exhibited a similar current density at 1.58 V versus RHE to the homometallic Ni-BHT. However, an increased actual Fe ratio resulted in a higher current density, with the $NiFe_{1:4}$-BHT (Fe ratio of 76.9%) achieving the highest current density. Conversely, the current density in the homometallic Fe-BHT was significantly lower than in the $NiFe_{1:4}$-BHT. This performance fluctuation indicates the unexpected synergetic effect that varies with the Fe ratio in the heterogeneous metal species. Notably, the overpotential required to reach 10 mA cm^{-2}_{geo} (= 140 A g^{-1}) was only 350 mV for the $NiFe_{1:4}$-BHT electrocatalyst (Figure 5a,c). This nonlinear trend can be explained by the variations in adsorption energy that would change with the Ni:Fe ratio in the material. This suggests that the $NiFe_{1:4}$-BHT would exhibit the most optimized adsorption energy for OER reactant, thus facilitating OER progress. According to the Sabatier principle, for beneficial catalytic performance, the adsorption between the catalyst site and the reactant should be neither too weak nor too strong.[18] In this viewpoint, the $NiFe_{1:4}$-BHT would feature the most optimized adsorption environment for OER intermediates and water molecules among the samples. This aspect will be further addressed in the subsequent section, using DFT calculations from the viewpoint of adsorption energy and energy barrier.

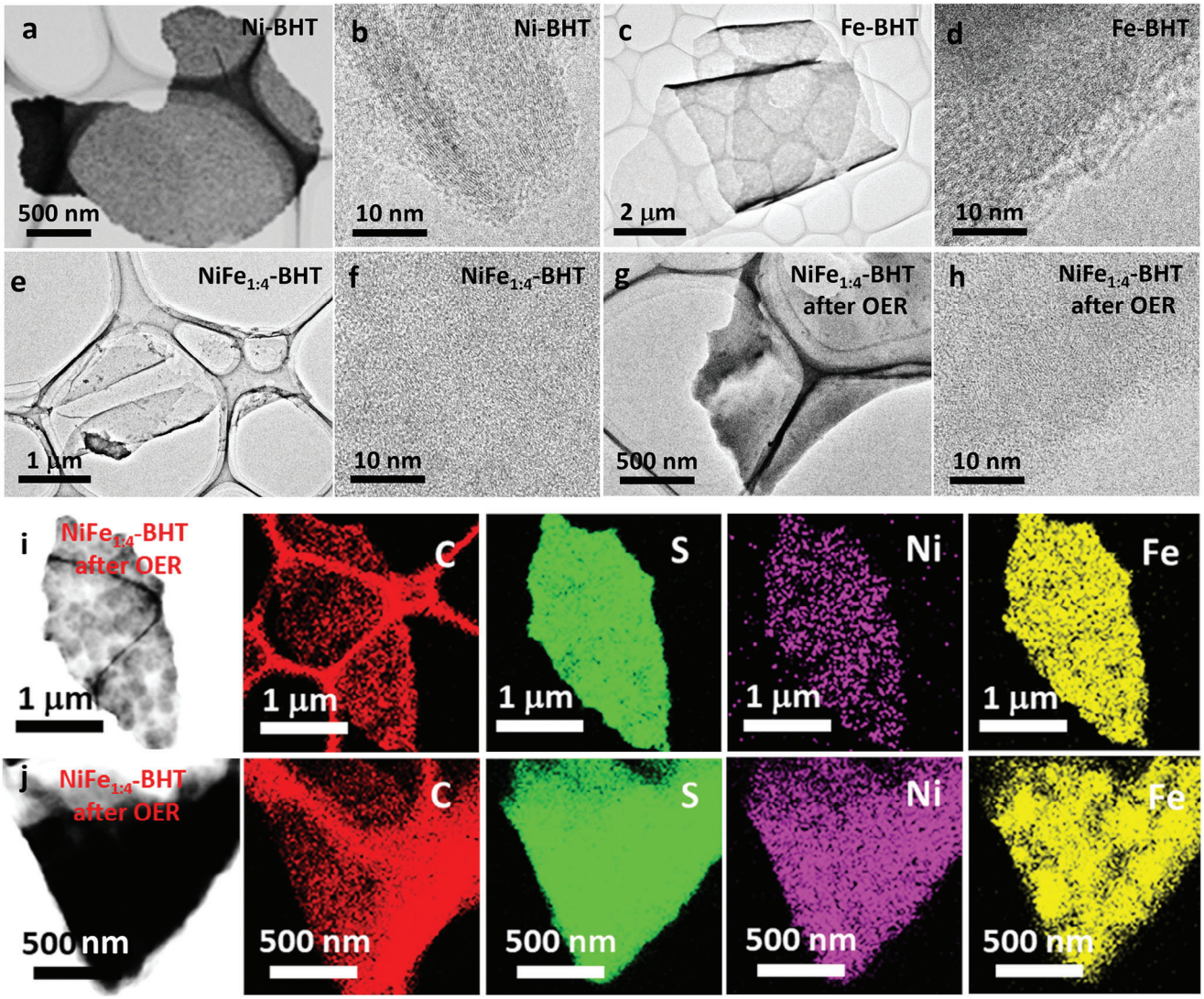

Figure 3. TEM images of a,b) the Ni-BHT, c,d) the Fe-BHT, e,f) the $NiFe_{1:4}$-BHT, and g,h) the $NiFe_{1:4}$-BHT 2DCF after OER measurements. i,j) The results of TEM-EDX mapping of the $NiFe_{1:4}$-BHT 2DCF after OER measurement in different selected areas and magnifications.

An analysis of intrinsic parameters, such as the Tafel slope, provides insight into the inherent kinetics of the electrocatalyst. The OER process under alkaline conditions can be described by the following four consecutive steps Equations (1)–(4):[19]

$$M + OH^- \rightleftharpoons M - OH + e^- \quad (1)$$

$$M - OH + OH^- \rightleftharpoons M - O + H_2O + e^- \quad (2)$$

$$M - O + OH^- \rightleftharpoons M - OOH + e^- \quad (3)$$

$$M - OOH + OH^- \rightleftharpoons M + H_2O + O_2 + e^- \quad (4)$$

Where M indicates an active site on the catalyst surface. One of the steps can be a rate-determining step of the OER process, depending on the electrocatalyst.[20] Tafel slope can be calculated in the following Equation (5);

$$\eta = a + b\log(j) \quad (5)$$

where η is a difference between the electrode and standard potentials (i.e, $\eta = E - E_0$), a is a constant, j means a current density, and b indicates the Tafel slope.

In several studies under alkaline conditions, the magnitude of Tafel slope has been utilized to evaluate the overall OER kinetics and predict the rate-determining steps in OER. A Tafel slope value is correlated to a specific rate-determining step according to the kinetic analysis. For example, a large Tafel slope of 120 mV dec^{-1} at low overpotential region can imply that the rate-determining step can be step (1), while a decrease in the Tafel slope can mean a shift of the rate-determining step to the other steps.[19] For instance, the Tefel slope of 100 mV dec^{-1} for the polycrystalline γ-FeO(OH) would denote step (2) (Equation (2)) as

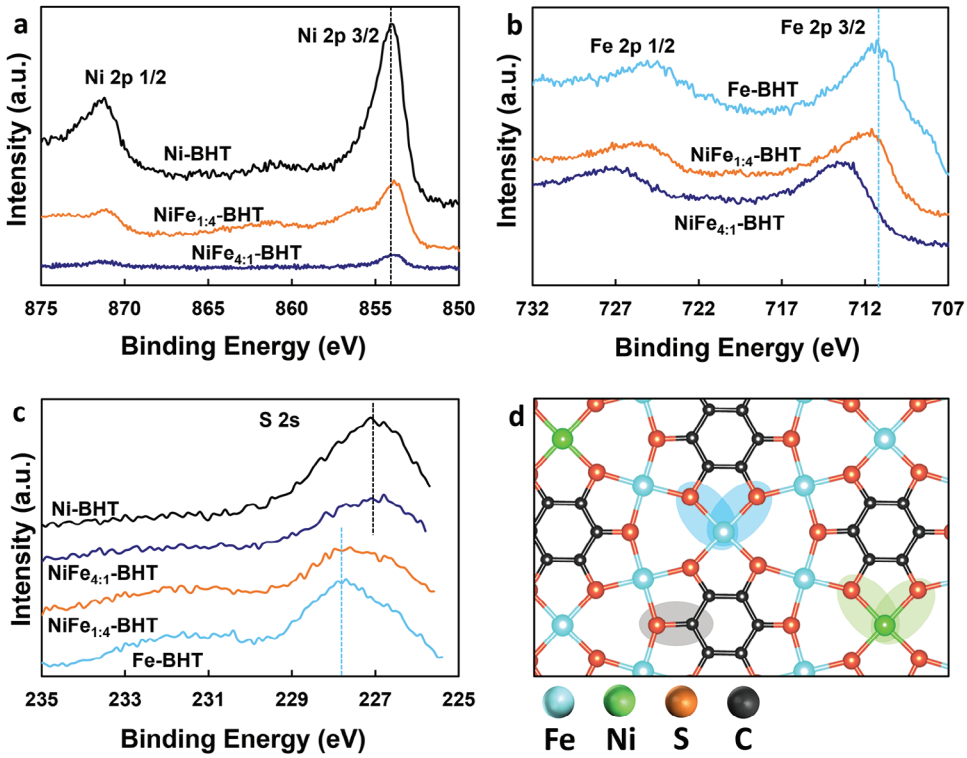

Figure 4. XPS spectra of a) Ni 2p region, b) Fe 2p region, and c) S 2s region of measured 2DCF. d) Schematic description of the molecular structure of the $NiFe_{x:y}$-BHT.

a rate-determining step, while a Tefel slope of 40 mV dec^{-1} would signify the step (3) (Equation 3) as a rate-determining step.[20] For instance, the Tafel slope of 40.9 mV dec^{-1} for a NiFe selenide catalyswas suggested that step (3) (Equation (3)) could be a rate-determining step.[20]

As shown in Figure S8 (Supporting Information), the $NiFe_{1:4}$-BHT exhibited the lowest Tafel slope of 25.3 mV dec^{-1} compared to that of the $NiFe_{3:2}$-BHT (38.8 mV dec^{-1}) and the Fe-BHT (79.8 mV dec^{-1}). Thus it can be concluded that the heterometallic $NiFe_{x:y}$-BHT can exhibit different OER kinetics than the homometallic Fe-BHT, and the $NiFe_{1:4}$-BHT would be an optimal condition for promoting the OER process. Furthermore, the lowest Tafel slope of the $NiFe_{1:4}$-BHT implies that the rate-determining step becomes closer to step (3) (Equation (3)), which would be the process of the formation of M-OOH from M—O.

Furthermore, the electrochemical impedance spectroscopy and the electrochemical surface area (ECSA) values further provide fundamental viewpoints on high electrochemical properties of the $NiFe_{1:4}$-BHT by showing the lowest charge transfer resistance and highest ECSA, which values are key to achieving better electrochemical properties (Figure S9a, Supporting Information). These results further substantiate the distinguished OER activity of $NiFe_{1:4}$-BHT. Figure S9b (Supporting Information) reveals that the structure of the $NiFe_{1:4}$-BHT loaded onto the carbon paper (the $NiFe_{1:4}$-BHT/CP) is stable in the alkaline electrolyte medium during a long-time operation. Figure S10a (Supporting Information) shows the linear sweep voltammetry curve of the $NiFe_{1:4}$-BHT/CP. The ex-situ Raman spectrum at different OER potentials (Figure S10b, Supporting Information), TEM images (Figure 3g,h), and TEM-EDX results (Figure 3i,j) confirmed no structural transformation in the $NiFe_{1:4}$-BHT, which even experienced a high OER potential, revealing its structural stability. Collectively, the performance of the $NiFe_{1:4}$-BHT (mass activity) is comparable to the state-of-the-art non-precious OER electrocatalysts and platinum-group-metal materials of RuO_2 and IrO_2 (Figure 5d; Table S2, Supporting Information).[2,17] The improved electrocatalytic performance of the $NiFe_{1:4}$-BHT can pave the way for industrial applications. For instance, its superior mass activity (140 A g^{-1}) will facilitate the efficient fabrication of an electrocatalytic material system that can be robust under industrial operation conditions (>500 mA cm^{-2}).

2.4. Analysis of OER Mechanism on $NiFe_{x:y}$-BHT

In order to uncover the reason for the superior electrochemical property of the $NiFe_{1:4}$-BHT compared to other Ni/Fe ratios, we constructed atomic models of the $NiFe_{x:y}$-BHT with different Ni/Fe ratios (1:5 and 5:1) and executed DFT calculations to assess the impact of these ratios on electronic properties and reaction mechanism. Figure S11a,b (Supporting Information) displays the monolayer structures utilized in this study, while Figure S12 (Supporting Information) presents the total energy variation as determined by DFT. This helped identify the most energetically favorable structures for the $NiFe_{1:5}$-BHT and the $NiFe_{5:1}$-BHT. **Figure 6a** presents a top view of the monolayer structures and the magnetic moment for each Ni or Fe atom. The magnetic moment of Fe atoms in the Fe-BHT, at 1.94 μB, markedly exceeds

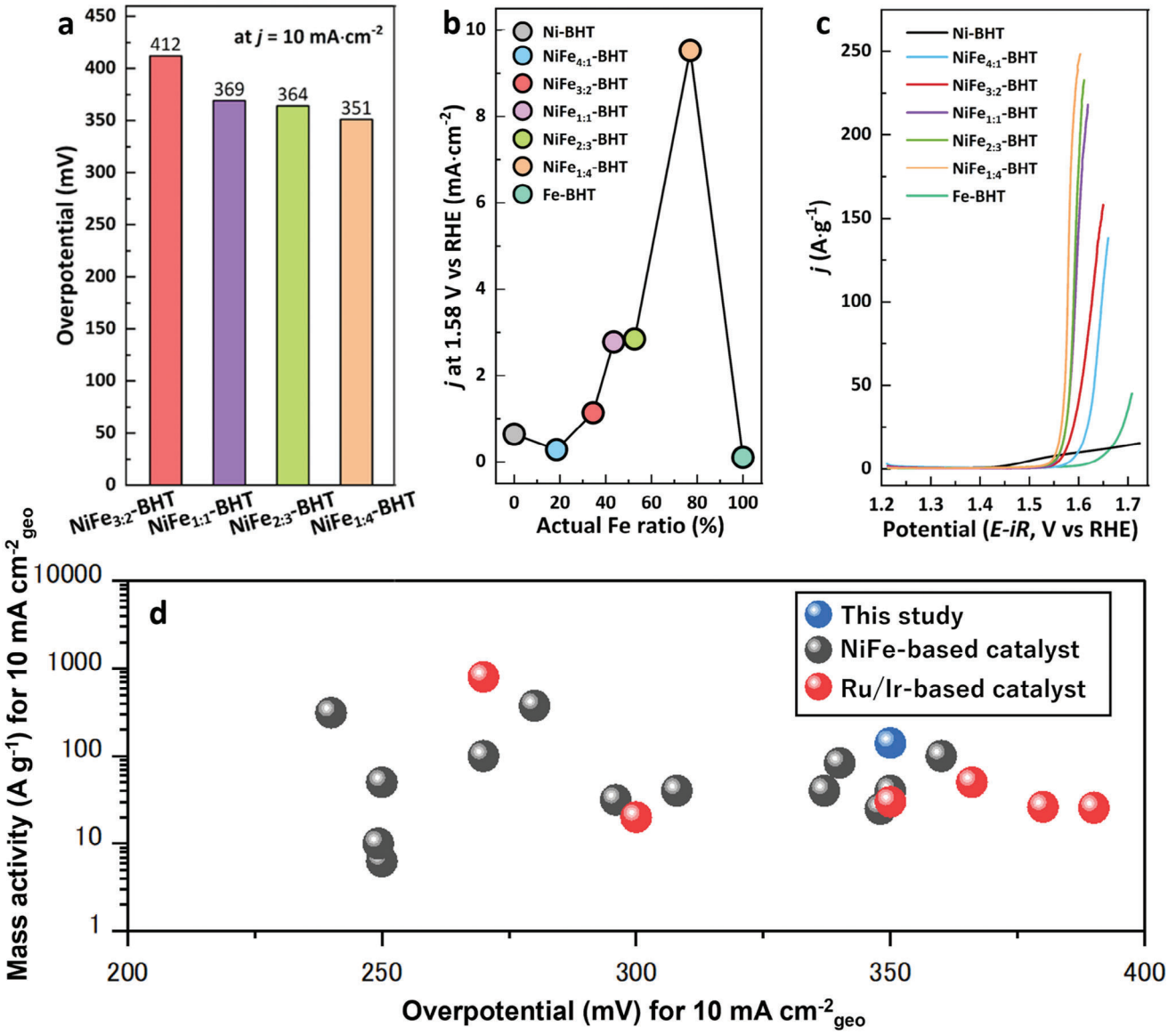

Figure 5. a) Overpotentials of the various $NiFe_{x:y}$-BHT 2DCF at a current density of 10 mA cm^{-2}. b) Current density obtained at 1.58 V versus RHE as a function of actual Fe ratio in metal species. c) Mass activity versus potential curves taken by linear sweep voltammogram technique for the Ni-BHT, $NiFe_{4:1}$-BHT, $NiFe_{3:2}$-BHT, $NiFe_{1:1}$-BHT, $NiFe_{2:3}$-BHT, $NiFe_{1:4}$-BHT and Fe-BHT 2DCF. For the collective comparison with other electrochemical results, this graph was edited from Figure S1 (Supporting Information) and placed in **Figure 5**. Mass activity versus potential curves taken by linear sweep voltammogram technique for the Ni-BHT, $NiFe_{4:1}$-BHT, $NiFe_{3:2}$-BHT, $NiFe_{1:1}$-BHT, $NiFe_{2:3}$-BHT, $NiFe_{1:4}$-BHT and Fe-BHT 2DCF. For the collective comparison with other electrochemical results, this graph was edited from Figure S1 (Supporting Information) and placed in Figure 5. d) Comparison of mass activity versus overpotential of state-of-the-art OER catalyst at 10 mA cm^{-2}_{geo}.[2c,17] The mass-loading for this study is 0.07 mg cm^{-2}_{geo}, and the electrolyte KOH solution (0.1 M, pH 13). (See Table S2, Supporting Information, for the detailed numerical values).

that of Ni atoms in the Ni-BHT, which is 0.41 μB. This heightened magnetic moment for Fe in the Fe-BHT arises from the asymmetry between spin-up and spin-down d-orbital partial density of states (PDOS), as depicted in Figure S13 (Supporting Information). Conversely, in the Ni-BHT, the PDOS between spin-up and spin-down is more balanced, resulting in a minimal magnetic moment. Additionally, in the $NiFe_{1:5}$-BHT and the $NiFe_{5:1}$-BHT, Fe atoms exhibit an enhanced magnetic moment of ≈2.3 μB, surpassing that of Fe atoms in Fe-BHT. The increased magnetic moment on the Fe atoms in the $NiFe_{1:5}$-BHT and $NiFe_{5:1}$-BHT can be attributed to spontaneous-spin-polarization induced by the presence of nearby Ni atoms.

Two key factors influencing the current density for $NiFe_{x:y}$-BHT were considered in this work: the adsorption tendency of OH on $NiFe_{x:y}$-BHT and the activation barrier through the OER pathway. Figure 6b presents the adsorption energy (E_{ad}) of OH on $NiFe_{x:y}$-BHT. Notably, the E_{ad} of the Fe-BHT (0.125 eV) is lower than that of Ni-BHT (0.608 eV). Additionally, on the $NiFe_{1:5}$-BHT and $NiFe_{5:1}$-BHT, all Fe atoms exhibit lower E_{ad} values than those of Ni atoms; 0.050 eV (Fe-atom) versus 1.072 eV (Ni-atom) and

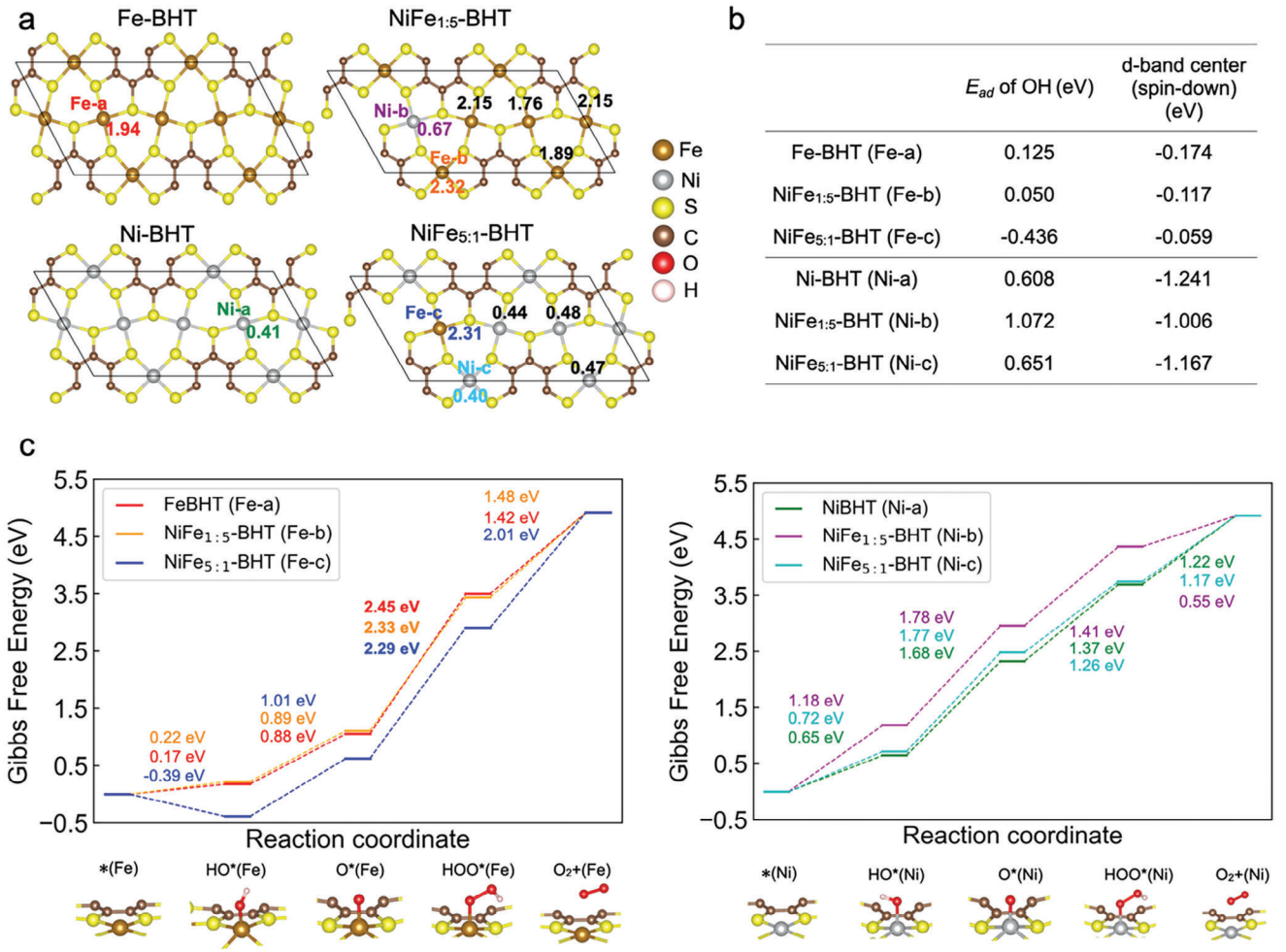

	E_{ad} of OH (eV)	d-band center (spin-down) (eV)
Fe-BHT (Fe-a)	0.125	-0.174
$NiFe_{1:5}$-BHT (Fe-b)	0.050	-0.117
$NiFe_{5:1}$-BHT (Fe-c)	-0.436	-0.059
Ni-BHT (Ni-a)	0.608	-1.241
$NiFe_{1:5}$-BHT (Ni-b)	1.072	-1.006
$NiFe_{5:1}$-BHT (Ni-c)	0.651	-1.167

Figure 6. Various physical properties of $NiFe_{x:y}$-BHT. a) illustrates the atomic configurations of $NiFe_{x:y}$BHT as viewed from above, with numerical labels denoting the magnetic moment of Ni and Fe atoms. b) presents the computed adsorption energy (E_{ad}) of OH on $NiFe_{x:y}$-BHT alongside the calculated d-band center. Only spin-down values are displayed, as they exhibit a more positive charge conducive to bonding. c) showcases the calculated Gibbs free energy diagram of $NiFe_{x:y}$BHT along the OER pathway, delineating four intermediate steps. The inserted numerical values represent the change in Gibbs free energy between consecutive steps.

−0.436 eV (Fe-atom) to 0.651 eV (Ni-atom), respectively. The relatively lower E_{ad} suggests that Fe atoms serve as the primary adsorption sites for the OER reactant, OH, rather than Ni atoms. Furthermore, upon introducing Ni atoms to Fe-BHT, the E_{ad} is notably reduced compared to Fe-BHT, indicating a stronger tendency and optimized condition for OH absorption on Fe atoms in $NiFe_{1:5}$-BHT and $NiFe_{5:1}$-BHT, potentially augmenting the current density. Figure 6b also displays the calculated d-band center. The calculated spin-down d-band center is found to be higher for Fe atoms than for Ni atoms, −0.174 and −1.241 eV, respectively. Additionally, Fe atoms in the $NiFe_{1:5}$-BHT and $NiFe_{5:1}$-BHT display an even more positive spin-down d-band center, −0.117 and −0.059 eV, respectively. The alteration in the d-band center correlates with the magnetic moment, as the high magnetic moment stems from the substantial difference between spin-up and spin-down d-states. A more positive d-band center is considered to result in stronger bonding between the surface and absorbed molecules according to the d-band theory.[4,21] Therefore, the lower E_{ad} of OH on highly active Fe atoms, characterized by a higher magnetic moment, in $NiFe_{1:5}$-BHT and $NiFe_{5:1}$-BHT can be attributed to the more positive d-band center, providing stronger bonding with OH.

Regarding the activation barrier in the OER pathway, the Gibbs free energy (G) of four intermediate steps: HO^*, O^*, HOO^*, and O_2, as previously studied:[12,19] were calculated and depicted in Figure 6c. For the Fe-BHT and the Ni-BHT, the largest ΔG is 2.45 and 1.68 eV for $O^* \rightarrow HOO^*$ and $HO^* \rightarrow O^*$, respectively, consistent with prior research.[12] The larger ΔG_{max} for the Fe-BHT implies a higher overpotential is necessary to make all steps' ΔG negative and spontaneous. This is also supported by work function calculations (Figure S11c, Supporting Information), where the work functions of the Ni-BHT and Fe-BHT are 5.10 and 4.47 eV, respectively. Thus, the Fermi level of the Fe-BHT versus the vacuum level is higher, indicating a weaker tendency to extract electrons from water molecules, leading to a higher overpotential compared to the Ni-BHT. Consequently, the Fe-BHT exhibits a higher overpotential than the Ni-BHT, in line with experimental results (Figure 5c). Moreover, ΔG_{max} of Fe atoms in

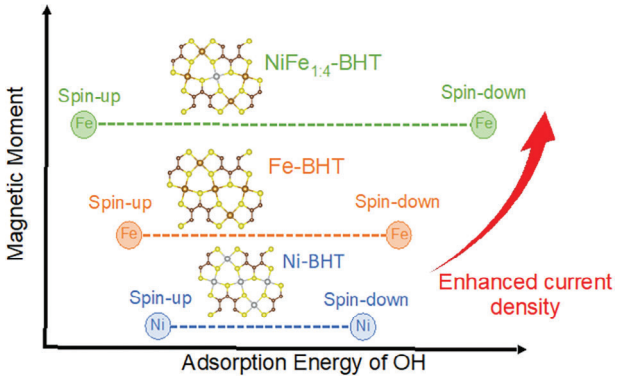

Figure 7. Schematic representation of the pivotal factors influencing OER performance in the $NiFe_{x:y}$-BHT materials.

the $NiFe_{1:5}$-BHT and the $NiFe_{5:1}$-BHT is reduced by over 0.1 to 2.33 eV and 2.29 eV, respectively, indicating lower overpotential compared to the Fe-BHT but still higher than Ni-BHT, consistent with our experimental results. The agreement between DFT predictions and empirical findings underscores the accuracy of our calculations in capturing the intrinsic electronic properties of these materials. The smaller ΔG_{max} on the $NiFe_{1:5}$-BHT and $NiFe_{5:1}$-BHT suggests a reduced activation barrier in the OER reaction, potentially enhancing the current density at the same applied potential. This reduced activation barrier can also be rationalized by the heightened magnetic moment of Fe atoms in the $NiFe_{1:5}$-BHT and $NiFe_{5:1}$-BHT. Previous research[6] has suggested that robust spin-polarization in transition metal atoms can enhance OER performance by lowering the energy barrier. This trend is evident in our calculations, as demonstrated above, where the energy barrier of $O^* \rightarrow HOO^*$ is reduced on Fe atoms with high magnetic moments in the $NiFe_{1:5}$-BHT and $NiFe_{5:1}$-BHT.

Through the foregoing analysis, it is evident that the primary reaction site is Fe, with Fe atoms in the $NiFe_{1:5}$-BHT and $NiFe_{5:1}$-BHT exhibiting even greater activity than those in Fe-BHT, as indicated by their low E_{ad} of OH and the lower activation barrier of $O^* \rightarrow HOO^*$. However, in experimental results, the $NiFe_{1:4}$-BHT demonstrates a higher current density compared to the $NiFe_{4:1}$-BHT and other $NiFe_{x:y}$-BHT compositions where the Fe content is lower than in $NiFe_{1:4}$-BHT, as depicted in Figure 5c. This discrepancy can be attributed to the abundance of highly active Fe sites. Despite the apparent higher activity of Fe atoms in $NiFe_{x:y}$-BHT compared to Fe-BHT, $NiFe_{1:4}$-BHT harbors more Fe atoms than other $NiFe_{x:y}$-BHT compositions, resulting in the highest current density among them. **Figure 7** shows the concepts of the key factors for OER performance revealed in this study.

3. Conclusion

In this study, we present the heterometallic π-d conjugated $NiFe_{1:4}$-BHT featuring spontaneous spin-polarization as an OER electrocatalyst. The $NiFe_{1:4}$-BHT demonstrated the most efficient OER activity among the samples of various Ni:Fe ratios, achieving a current density of up to 10 mA cm^{-2} at an overpotential of 350 mV. The DFT calculations, aligning closely with experimental data, elucidated the electronic and structural nuances influencing OER activity. The key findings in this study illustrate the crucial role of magnetic moments in Fe atoms, the influence of adsorption energy of reactant OH, and the quantity of reactive Fe atoms in determining the optimal performance of the $NiFe_{1:4}$-BHT by emerging spontaneous-spin-polarization. This study offers not only a new strategy to realize 2DCF with abundant metal species as a distinguished oxygen-evolving electrocatalysts but also shows that 2DCFs as a platform to design materials with unexpected functions. We anticipate that this study will inspire the material science community and also other a wide spectrum of research fields to establish green science and technology at an affordable cost, ultimately contributing to developing human society in the 21st century.

Supporting Information

Supporting Information is available from the Wiley Online Library or from the author.

Acknowledgements

The GIWAXS experiments were performed at BL05XU in SPring-8 (Hyogo, Japan) with the approval of RIKEN. XPS measurements were supported by the Advanced Research Infrastructure for Materials and Nanotechnology in Japan (ARIM) of the Ministry of Education, Culture, Sports, Science and Technology (MEXT) (JPMXP12-A-23-UT-0025). This work was supported by the MEXT Program: Data Creation and Utilization-Type Material Research and Development Project Grant Number JPMXP1122712807. The TEM observations were supported by Prof. Y. Idemoto (Department of Pure and Applied Chemistry, Tokyo University of Science) and Dr. T. Ichihashi (Research Equipment Centre, Tokyo University of Science). Several experiments were conducted, and corresponding figures were provided by Dr. D. Xia. The authors are thankful to Dr. K. Tsukagoshi for the fruitful discussions. The authors gratefully acknowledge the financial support from JSPS KAKENHI Grant Number 19H05460, the National Science and Technology Council (NSTC) of Taiwan under the project (MOST 110-2222-E-006-014-MY3, 112-2923-E-006-004) and in part by the Higher Education Sprout Project, Ministry of Education, to the Headquarters of University Advancement at National Cheng Kung University (NCKU). Additionally, the authors thank the National Center for High-performance Computing (NCHC) for providing computational and storage resources.

Conflict of Interest

The authors declare no conflict of interest.

Data Availability Statement

The data that support the findings of this study are available from the corresponding author upon reasonable request.

Keywords

bimetallic p-d conjugation, coordination frameworks, electrocatalysts, oxygen evolution reaction, spin-polarization

Received: March 22, 2024
Revised: April 30, 2024
Published online:

[1] a) M. Chatenet, B. G. Pollet, D. R. Dekel, F. Dionigi, J. Deseure, P. Millet, R. D. Braatz, M. Z. Bazant, M. Eikerling, I. Staffell, P. Balcombe, Y. Shao-Horn, H. Schäfer, *Chem. Soc. Rev.* **2022**, *51*, 4583; b) W. Hoisang, K. Sakaushi, *Curr. Opin. Electrochem.* **2022**, *36*, 101136.

[2] a) T. Reier, M. Oezaslan, P. Strasser, *ACS Catal.* **2012**, *2*, 1765; b) E. Fabbri, T. J. Schmidt, *ACS Catal.* **2018**, *8*, 9765; c) J. Kibsgaard, I. Chorkendorff, *Nat. Energy* **2019**, *4*, 430.

[3] a) H. Tamura, C. Iwakura, *Int. J. Hydrog. Energy* **1982**, *7*, 857; b) J. O. M. Bockris, T. Otagawa, *J. Electrochem. Soc.* **1984**, *131*, 290; c) S. Trasatti, *Electrochim. Acta* **2000**, *45*, 2377; d) C. C. L. McCrory, S. Jung, J. C. Peters, T. F. Jaramillo, *J. Am. Chem. Soc.* **2013**, *135*, 16977; e) K. Sakaushi, M. Antonietti, *Acc. Chem. Res.* **2015**, *48*, 1591; f) W. T. Hong, M. Risch, K. A. Stoerzinger, A. Grimaud, J. Suntivich, Y. Shao-Horn, *Energy Environ. Sci.* **2015**, *8*, 1404; g) F. Dionigi, P. Strasser, *Adv. Energy Mater.* **2016**, *6*, 1600621; h) F. Lyu, Q. Wang, S. M. Choi, Y. Yin, *Small* **2019**, *15*, 1804201; i) A. Li, H. Ooka, N. Bonnet, T. Hayashi, Y. Sun, Q. Jiang, C. Li, H. Han, R. Nakamura, *Angew. Chem., Int. Ed.* **2019**, *58*, 5054; j) K. Sakaushi, W. Hoisang, R. Tamura, *ACS Cent. Sci.* **2023**, *9*, 2216.

[4] a) H. Gerischer, *Z. Phys. Chem.* **1956**, *8*, 137; b) R. Parsons, *Trans. Faraday Soc.* **1958**, *54*, 1053; c) I. C. Man, H.-Y. Su, F. Calle-Vallejo, H. A. Hansen, J. I. Martínez, N. G. Inoglu, J. Kitchin, T. F. Jaramillo, J. K. Nørskov, J. Rossmeisl, *ChemCatChem* **2011**, *3*, 1159; d) J. K. Nørskov, F. Abild-Pedersen, F. Studt, T. Bligaard, *Proc. Natl. Acad. Sci. U.S.A.* **2011**, *108*, 937; e) K. Sakaushi, T. Kumeda, S. Hammes-Schiffer, M. M. Melander, O. Sugino, *Phys. Chem. Chem. Phys.* **2020**, *22*, 19401; f) K. Sakaushi, *Phys. Chem. Chem. Phys.* **2020**, *22*, 11219; g) H. Ooka, M. E. Wintzer, R. Nakamura, *ACS Catal.* **2021**, *11*, 6298.

[5] A. Fujishima, K. Honda, *Nature* **1972**, *238*, 37.

[6] a) T. Z. Fahidy, *J. Appl. Electrochem.* **1983**, *13*, 553; b) S. Mohanta, T. Z. Fahidy, *Can. J. Chem. Eng.* **1972**, *50*, 248; c) G. Hinds, F. E. Spada, J. M. D. Coey, T. R. Ní Mhíocháin, M. E. G. Lyons, *J. Phys. Chem. B* **2001**, *105*, 9487; d) D. Fernández, Z. Diao, P. Dunne, J. M. D. Coey, *Electrochim. Acta* **2010**, *55*, 8664; e) F. A. Garcés-Pineda, M. Blasco-Ahicart, D. Nieto-Castro, N. López, J. R. Galán-Mascarós, *Nat. Energy* **2019**, *4*, 519; f) S. S. Bhargava, D. Azmoodeh, X. Chen, E. R. Cofell, A. M. Esposito, S. Verma, A. A. Gewirth, P. J. A. Kenis, *ACS Energy Lett.* **2021**, *6*, 2427; g) X. Ren, T. Wu, Y. Sun, Y. Li, G. Xian, X. Liu, C. Shen, J. Gracia, H.-J. Gao, H. Yang, Z. J. Xu, *Nat. Commun.* **2021**, *12*, 2608; h) L. Li, J. Zhou, X. Wang, J. Gracia, M. Valvidares, J. Ke, M. Fang, C. Shen, J.-M. Chen, Y.-C. Chang, C.-W. Pao, S.-Y. Hsu, J.-F. Lee, A. Ruotolo, Y. Chin, Z. Hu, X. Huang, Q. Shao, *Adv. Mater.* **2023**, *35*, 2302966; i) L. Lin, Y. Xu, Y. Han, R. Xu, T. Wang, Z. Sun, Z. Yan, *J. Am. Chem. Soc.* **2024**, *146*, 7363.

[7] a) T. Kambe, R. Sakamoto, K. Hoshiko, K. Takada, M. Miyachi, J.-H. Ryu, S. Sasaki, J. Kim, K. Nakazato, M. Takata, H. Nishihara, *J. Am. Chem. Soc.* **2013**, *135*, 2462; b) T. Kambe, R. Sakamoto, T. Kusamoto, T. Pal, N. Fukui, K. Hoshiko, T. Shimojima, Z. Wang, T. Hirahara, K. Ishizaka, S. Hasegawa, F. Liu, H. Nishihara, *J. Am. Chem. Soc.* **2014**, *136*, 14357.

[8] K. Sakaushi, H. Nishihara, *Acc. Chem. Res.* **2021**, *54*, 3003.

[9] a) L. S. Xie, G. Skorupskii, M. Dincă, *Chem. Rev.* **2020**, *120*, 8536; b) X. Huang, P. Sheng, Z. Tu, F. Zhang, J. Wang, H. Geng, Y. Zou, C.-a. Di, Y. Yi, Y. Sun, W. Xu, D. Zhu, *Nat. Commun.* **2015**, *6*, 7408; c) M. G. Campbell, D. Sheberla, S. F. Liu, T. M. Swager, M. Dincă, *Angew. Chem., Int. Ed.* **2015**, *54*, 4349; d) J.-H. Dou, L. Sun, Y. Ge, W. Li, C. H. Hendon, J. Li, S. Gul, J. Yano, E. A. Stach, M. Dincă, *J. Am. Chem. Soc.* **2017**, *139*, 13608.

[10] a) M. Ko, L. Mendecki, K. A. Mirica, *Chem. Commun.* **2018**, *54*, 7873; b) M. Wang, R. Dong, X. Feng, *Chem. Soc. Rev.* **2021**, *50*, 2764; c) G. Chakraborty, I.-H. Park, R. Medishetty, J. J. Vittal, *Chem. Rev.* **2021**, *121*, 3751.

[11] a) K. Wada, K. Sakaushi, S. Sasaki, H. Nishihara, *Angew. Chem., Int. Ed.* **2018**, *57*, 8886; b) M. Amores, K. Wada, K. Sakaushi, H. Nishihara, *J. Phys. Chem. C* **2020**, *124*, 9215; c) Z. Wu, D. Adekoya, X. Huang, M. J. Kiefel, J. Xie, W. Xu, Q. Zhang, D. Zhu, S. Zhang, *ACS Nano* **2020**, *14*, 12016; d) D. Xia, K. Sakaushi, A. Lyalin, K. Wada, S. Kumar, M. Amores, H. Maeda, S. Sasaki, T. Taketsugu, H. Nishihara, *Small* **2022**, *18*, 2202861; e) J. M. Wrogemann, M. J. Lüther, P. Bärmann, M. Lounasvuori, A. Javed, M. Tiemann, R. Golnak, J. Xiao, T. Petit, T. Placke, M. Winter, *Angew. Chem., Int. Ed.* **2023**, *62*, e202303111.

[12] a) E. M. Miner, T. Fukushima, D. Sheberla, L. Sun, Y. Surendranath, M. Dincă, *Nat. Commun.* **2016**, *7*, 10942; b) X. Sun, K.-H. Wu, R. Sakamoto, T. Kusamoto, H. Maeda, X. Ni, W. Jiang, F. Liu, S. Sasaki, H. Masunaga, H. Nishihara, *Chem. Sci.* **2017**, *8*, 8078; c) X. Fan, S. Tan, J. Yang, Y. Liu, W. Bian, F. Liao, H. Lin, Y. Li, *ACS Energy Lett.* **2022**, *7*, 343.

[13] a) X. Zhang, Y. Zhou, B. Cui, M. Zhao, F. Liu, *Nano Lett.* **2017**, *17*, 6166; b) X. Huang, S. Zhang, L. Liu, L. Yu, G. Chen, W. Xu, D. Zhu, *Angew. Chem., Int. Ed.* **2018**, *57*, 146; c) T. Takenaka, K. Ishihara, M. Roppongi, Y. Miao, Y. Mizukami, T. Makita, J. Tsurumi, S. Watanabe, J. Takeya, M. Yamashita, K. Torizuka, Y. Uwatoko, T. Sasaki, X. Huang, W. Xu, D. Zhu, N. Su, J.-G. Cheng, T. Shibauchi, K. Hashimoto, *Sci. Adv.* **2021**, *7*, eabf3996.

[14] a) M. K. Smith, K. A. Mirica, *J. Am. Chem. Soc.* **2017**, *139*, 16759; b) M. Ko, L. Mendecki, A. M. Eagleton, C. G. Durbin, R. M. Stolz, Z. Meng, K. A. Mirica, *J. Am. Chem. Soc.* **2020**, *142*, 11717.

[15] R. Toyoda, N. Fukui, D. H. L. Tjhe, E. Selezneva, H. Maeda, C. Bourgès, C. M. Tan, K. Takada, Y. Sun, I. Jacobs, K. Kamiya, H. Masunaga, T. Mori, S. Sasaki, H. Sirringhaus, H. Nishihara, *Adv. Mater.* **2022**, *34*, 2106204.

[16] C. M. Tan, M. Horikawa, N. Fukui, H. Maeda, S. Sasaki, K. Tsukagoshi, H. Nishihara, *Chem. Lett.* **2020**, *50*, 576.

[17] a) Y. Gorlin, T. F. Jaramillo, *J. Am. Chem. Soc.* **2010**, *132*, 13612; b) M. Gong, Y. Li, H. Wang, Y. Liang, J. Z. Wu, J. Zhou, J. Wang, T. Regier, F. Wei, H. Dai, *J. Am. Chem. Soc.* **2013**, *135*, 8452; c) M. W. Louie, A. T. Bell, *J. Am. Chem. Soc.* **2013**, *135*, 12329; d) M.-R. Gao, X. Cao, Q. Gao, Y.-F. Xu, Y.-R. Zheng, J. Jiang, S.-H. Yu, *ACS Nano* **2014**, *8*, 3970; e) Z. Lu, W. Xu, W. Zhu, Q. Yang, X. Lei, J. Liu, Y. Li, X. Sun, X. Duan, *Chem. Commun.* **2014**, *50*, 6479; f) X. Lu, C. Zhao, *Nat. Commun.* **2015**, *6*, 1; g) L. Qian, Z. Lu, T. Xu, X. Wu, Y. Tian, Y. Li, Z. Huo, X. Sun, X. Duan, *Adv. Energy Mater.* **2015**, *5*, 1500245; h) C. Tang, H. S. Wang, H. F. Wang, Q. Zhang, G. L. Tian, J. Q. Nie, F. Wei, *Adv. Mater.* **2015**, *27*, 4516; i) H. Wang, H.-W. Lee, Y. Deng, Z. Lu, P.-C. Hsu, Y. Liu, D. Lin, Y. Cui, *Nat. Commun.* **2015**, *6*, 7261; j) Y. Xu, Y. Hao, G. Zhang, Z. Lu, S. Han, Y. Li, X. Sun, *RSC Adv.* **2015**, *5*, 55131; k) X. Zhu, C. Tang, H.-F. Wang, Q. Zhang, C. Yang, F. Wei, *J. Mater. Chem. A* **2015**, *3*, 24540; l) F. Dionigi, T. Reier, Z. Pawolek, M. Gliech, P. Strasser, *ChemSusChem* **2016**, *9*, 962; m) Y. Gao, X. Liu, G. Yang, *Nanoscale* **2016**, *8*, 5015; n) D.-c. Xia, L. Zhou, S. Qiao, Y. Zhang, D. Tang, J. Liu, H. Huang, Y. Liu, Z. Kang, *Mater. Res. Bull.* **2016**, *74*, 441; o) Y. Pi, Q. Shao, P. Wang, J. Guo, X. Huang, *Adv. Funct. Mater.* **2017**, *27*, 1700886; p) S. Yuan, J. Peng, B. Cai, Z. Huang, A. T. Garcia-Esparza, D. Sokaras, Y. Zhang, L. Giordano, K. Akkiraju, Y. G. Zhu, R. Hübner, X. Zou, Y. Román-Leshkov, Y. Shao-Horn, *Nat. Mater.* **2022**, *21*, 673.

[18] D.-Y. Kuo, H. Paik, J. Kloppenburg, B. Faeth, K. M. Shen, D. G. Schlom, G. Hautier, J. Suntivich, *J. Am. Chem. Soc.* **2018**, *140*, 17597.

[19] a) T. Shinagawa, A. T. Garcia-Esparza, K. Takanabe, *Sci. Rep.* **2015**, *5*, 13801; b) C. Iwakura, K. Fukuda, H. Tamura, *Electrochim. Acta* **1976**, *21*, 501.

[20] M. Chen, N. Kitiphatpiboon, C. Feng, A. Abudula, Y. Ma, G. Guan, *eScience* **2023**, *3*, 100111.

[21] a) B. Hammer, J. K. Nørskov, *Surf. Sci.* **1995**, *343*, 211; b) Z. Du, K. Deng, E. Kan, C. Zhan, *Phys. Chem. Chem. Phys.* **2023**, *25*, 13913; c) L. Hu, F. Wang, Y. Jing, *J. Phys. Chem. Lett.* **2023**, *14*, 11429.